



Repositorio Institucional de la Universidad Autónoma de Madrid

<https://repositorio.uam.es>

Esta es la **versión de autor** del artículo publicado en:

This is an **author produced version** of a paper published in:

Journal of the American Chemical Society 141.41 (2019): 16432-16438

DOI: <https://doi.org/10.1021/jacs.9b07868>

Copyright: © 2019 American Chemical Society

El acceso a la versión del editor puede requerir la suscripción del recurso

Access to the published version may require subscription

Noncovalent Synthesis of Self-assembled Nanotubes through Decoupled Hierarchical Cooperative Processes

Violeta Vázquez-González,[†] Maria J. Mayoral,[†] Raquel Chamorro,[†] Marco M. R. M. Hendrix,[‡] Ilja K. Voets,[‡] David González-Rodríguez^{†,‡,*}

[†] Organic Chemistry Department, Universidad Autónoma de Madrid, 28049 Madrid, Spain

[‡] Chemical Engineering and Chemistry & Institute for Complex Molecular Systems, Eindhoven University of Technology, Eindhoven, The Netherlands

[#] Institute for Advanced Research in Chemical Sciences (IAdChem), Campus de Cantoblanco, 28049 Madrid

KEYWORDS. *Supramolecular Chemistry, Supramolecular Polymerization, Self-assembled Nanotubes, Cooperativity.*

ABSTRACT: Due to their wide number of biological functions and potential applications, self-assembled nanotubes constitute highly relevant targets in noncovalent synthesis. Herein, we introduce a novel approach to produce supramolecular nanotubes with defined inner and outer diameters from rigid rod-like monomers programmed with complementary nucleobases through two distinct, decoupled cooperative process of different hierarchy and acting in orthogonal directions: chelate cooperativity, responsible for the formation of robust Watson-Crick H-bonded cyclic tetramers, and nucleation-growth cooperative polymerization.

INTRODUCTION

Noncovalent synthesis aims at the production of well-defined nanostructures, often mimicking those found in the natural world, and relies both on noncovalent interactions and cooperative effects between chemically programmed molecules.¹⁻³ One of the most appealing noncovalent synthetic targets are self-assembled nanotubes, due to their nanoscale dimensions, with inner cavities in the attoliter regime, their large variety of biological functions, illustrated by tube-forming proteins like tubulin or gramicidin,^{4,5} and their potential applications⁶⁻¹² in chemo- and size-selective encapsulation, transport, or catalysis. These cylindrical architectures can be formed from rationally designed molecules of different nature and through manifold approaches, that in many cases encompass multi-step pathways of increasing hierarchy.¹³⁻¹⁷

One of these approaches involves the combination of two hierarchical processes that are strongly coupled (Figure 1a; left). First, the association of dendron-shaped molecules with self-complementary H-bonding faces leads to rosette-like macrocycles and, as soon as these transient intermediates are formed, a stacking process is triggered in the orthogonal direction.¹⁸⁻²¹ The most popular building blocks employed here contain heterocyclic head groups like guanine,^{22,23} cyanuric/barbituric acid,^{24,25} melamine/diaminotriazine,²⁶ their combination,^{27,28} or pyrimido[4,5-d]pyrimidine derivatives.^{29,30} This strategy can be implemented in aqueous or organic media with molecules carrying diverse external functions. However, it affords little control on pore dimensions and function, and the resulting

nanotubes typically have small pores, able in the best case to accommodate ions or very small molecules.

Here we introduce a related strategy for the synthesis of self-assembled nanotubes that is based on a novel molecular design, involving rigid rod-like monomers that interact through their edges in a defined 90° geometry (Figure 1a; right). Specifically, our monomer structure (**GC**; Figure 1b) comprises complementary guanine (G) and cytosine (C) nucleobases linked by linear, π -conjugated spacers. The bases are also equipped with benzylic wedges substituted with long alkyl tails, so as to enhance solubility in apolar solvents, and with a peripheral amide group. This molecular design allowed to control self-assembly through two orthogonal cooperative events of different hierarchy, as shown in Figure 1c, that can be now efficiently *decoupled*. First, *chelate cooperativity* is responsible for the formation of unstrained cyclic tetramers through G:C Watson-Crick H-bonding interactions,³¹ as demonstrated previously with related molecules bearing bulky riboses.³²⁻³⁸ After these planar macrocycles are generated quantitatively, a polymerization process, that occurs through a *nucleation-growth* mechanism and is guided by π - π and H-bonding interactions along the stacking axis, can be triggered by a change in experimental conditions. Hence, both cooperative processes are independent and self-assembly can be controlled either at the cycle stage or at the polymer stage. Since the “supramonomer” is cyclic in nature, the resulting polymer is tubular, with precisely defined inner and outer diameters.

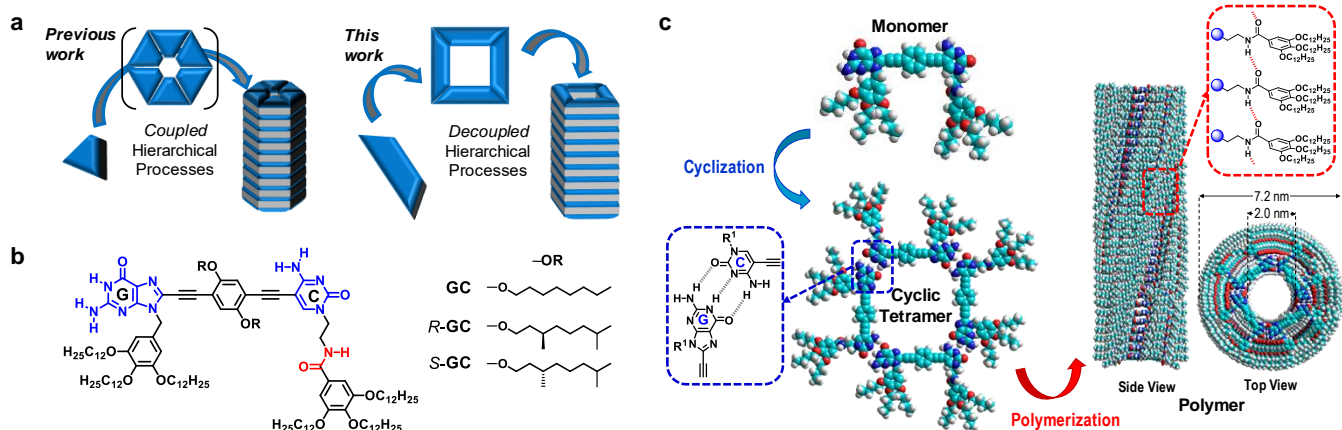


Figure 1. (a) Previous and current approaches to self-assembled nanotubes from cyclic species. (b) Structure of achiral GC and chiral R-GC/S-GC molecules. (c) Scheme of the two-step self-assembly of dinucleobase monomers into nanotubes. Side alkyl tails were shortened/removed in the model for the sake of clarity.

RESULTS AND DISCUSSION

Monomer-Cyclic Tetramer Equilibrium. The association state of GC is, as expected, strongly dependent on the H-bonding competing ability of the solvent environment. Highly polar solvents like DMF or DMAC are able to produce full dissociation at concentrations below 10^{-3} M. Moving to solvents of intermediate polarity,³² like THF, allowed us to monitor the monomer (GC)-cyclic tetramer (cGC_4) equilibrium at concentrations between 10^{-2} - 10^{-5} M by 1H NMR, absorption, CD and emission spectroscopies. Figure 2a shows the evolution of the GC aromatic 1H signals as a function of temperature at 10^{-4} M in THF- D_8 (see Figures S1A-B for additional 1H NMR spectra at different temperatures and concentrations). As the temperature decreases from 323 to 268 K, the GC monomer signals (rods) decrease in intensity at the expense of the cGC_4 signals (squares). H-bonding between G and C nucleobases was confirmed by the characteristic downfield shift of the G-amide and the C-amine proton signals to 13.2 and 10.3 ppm, respectively, as well as by NOESY cross-peaks between these two H-bonded protons (Figures 2b and S1C). It is interesting to note that both GC and cGC_4 species are in slow exchange at the NMR timescale and that the shape and position of the 1H signals do not change much with temperature or concentration,³² which underlines the slow dynamics and *all-or-nothing* behavior of this macrocyclization process.

The 1H NMR data can be overlapped with optical spectroscopy techniques, and Figures 2c-e display, respectively, the absorption, CD and emission changes that occur at 10^{-4} M in THF as a function of temperature. Upon cooling, GC cyclotetramerization is promoted and a single, rigid conformation, that maintains the two Watson-Crick edges pointing in the same direction, is fixed.³²⁻³⁵ This is typically monitored by: 1) a red-shift in absorbance with a characteristic new maximum at 420 nm; 2) a decrease in emission intensity and a marked red-shift from 439 nm (GC) to 525 nm (cGC_4); and 3) a CD Cotton effect, positive for $cS-GC_4$ and negative for $cR-GC_4$, with zero-crossing at 434 nm. Figures S1D-E contain additional temperature- and concentration-dependent spectra in THF.³²⁻³⁵

Such spectroscopy changes can be used to determine the molar fraction of GC molecules associated as cGC_4 (χ_T) as a function of temperature (Figure 2f) or concentration (Figure 2g). The cyclization trends obtained from NMR and CD measurements at the same concentrations show an excellent agreement. Fitting the NMR data to a cyclotetramerization process afforded the corresponding equilibrium constants (K_T ; see S. I.), from which the effective molarity (EM) values could be calculated as $K_T = EM \cdot K_{G:C}^4$ (Table 1a and S1), where $K_{G:C}$ is the reference association constant between nucleobases in THF.³²

Table 1. Thermodynamic parameters calculated for GC upon (a) cyclotetramerization, (b) polymerization as a function of solvent composition, and (c) polymerization as a function of temperature.

a	$K_{G:C}^{[a]}/M^{-1}$	$K_T^{[b]}/M^{-3}$	$EM^{[c]}/M$	$\Delta H_T^{[d]}/kJ \cdot mol^{-1}$	$\Delta S_T^{[e]}/J \cdot mol^{-1} \cdot K^{-1}$
	$1.1 \cdot 10^3$	$3.4 \cdot 10^{12}$	2.3	-173.4	-331.2
b	$\Delta G^\circ [f]/kJ \cdot mol^{-1}$		$m^{[g]}/kJ \cdot mol^{-1}$		$\sigma^{[h]}$
	-34.9 ± 0.5		90 ± 9		0.19 ± 0.03
c	$K_n^{[i]}/M^{-1}$	$K_e^{[j]}/M^{-1}$	$\sigma^{[k]}$	$\Delta H^{o[l]}/kJ \cdot mol^{-1}$	$\Delta S^{o[m]}/J \cdot mol^{-1} \cdot K^{-1}$
	$4.02 \cdot 10^4$	$1.34 \cdot 10^5$	$3.0 \cdot 10^{-4}$	-116.6 ± 3	-290 ± 10

[a] Reference G:C association constant. [b] Cyclotetramerization constant. [c] Effective molarity calculated as: $EM = K_T / K_{G:C}^4$. [d] Cyclotetramerization enthalpy and [e] entropy. [f] Gibbs free energy, [g] m parameter and [h] degree of cooperativity of the polymerization process observed by increasing V_a . [i] Nucleation and [j] elongation constants, [k] cooperativity factor, and elongation [l] enthalpy and [m] entropy of the polymerization process observed by decreasing T .

Using these calculated EM and $K_{G:C}$ values, we built speciation curves in which monomer, cyclic tetramer and small open oligomers were included. These curves, in which the relative distribution of species is represented as a function of overall concentration, illustrate graphically the *all-or-nothing* process observed in solution, where mostly GC monomer (green) and cGC_4 macrocycles (purple) are in equilibrium, and the participation of small open

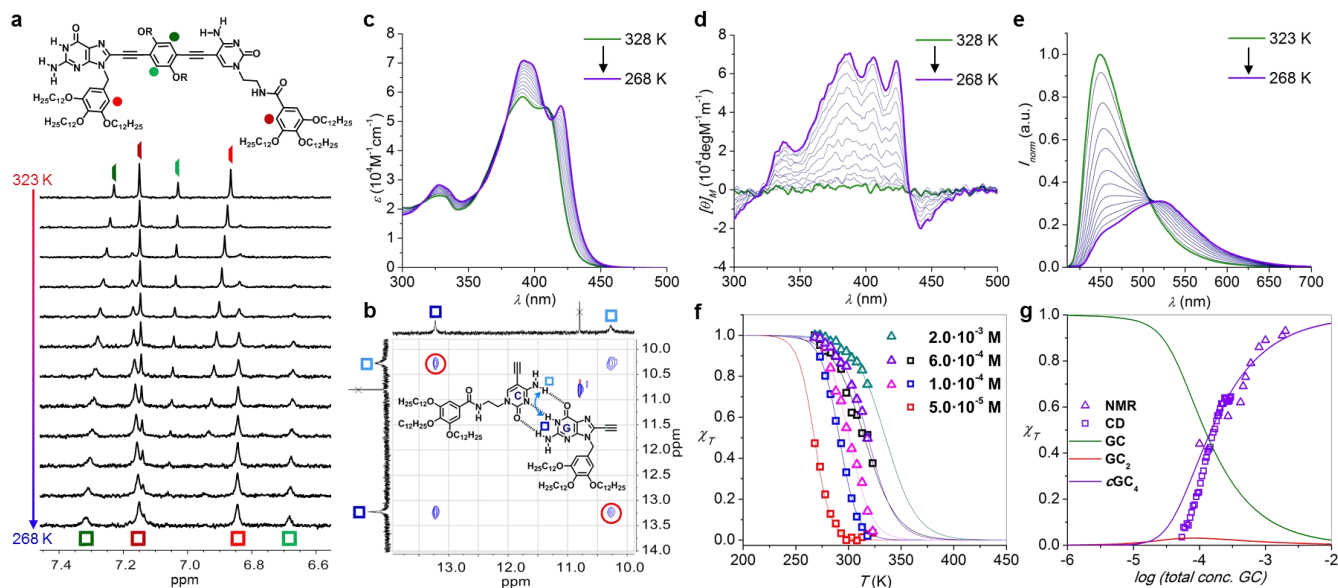


Figure 2. Cyclotetramerization. Changes observed in the (a) ^1H NMR, (c) absorption (d) CD and (e) emission spectra as a function of temperature for $1.0 \cdot 10^{-4}$ M solutions of GC in THF- D_8 (a) or *R*-GC in THF (c-e). (b) NOESY NMR spectrum at $\tau_m = 0$ ms of GC ($[\text{GC}] = 2.0 \cdot 10^{-3}$ M, 298 K) showing cross-peaks between H-bonded G and C protons. (f-g) Representation of the molar fraction of GC molecules associated as $c\text{GC}_4$ cycles (χ_T) calculated by ^1H NMR (triangles) or CD (squares) as a function of (f) the temperature at different concentrations or (g) the total concentration at 298 K. In (g) the relative abundance of GC, $c\text{GC}_4$ and open oligomers (like GC_2) was simulated (solid lines) using $K_{\text{GC}} = 1.1 \cdot 10^3 \text{ M}^{-1}$ and $EM = 2$ M.

oligomers (like dimer GC_2 ; in red) is insignificant. Furthermore, these simulated curves overlap quite nicely the experimental dilution data measured by ^1H NMR and CD, which corroborates the high chelate cooperativity calculated for this system. On the other hand, a Van't Hoff representation of the temperature-dependent data provided the enthalpic (ΔH_T) and entropic (ΔS_T) changes associated to the cyclization process in THF. These values are also displayed in Tables 1a and S1.

Similar analyses to those performed in THF were made in less-competing aromatic solvents like chlorobenzene or toluene (see Section S2), where K_{GC} increases considerably^{39,40} and the equilibrium is further shifted to the cycle side.

Cyclic Tetramer-Polymer Equilibrium. We then proceeded to force further aggregation by employing highly apolar alkane media, like methylcyclohexane (MCH), heptane or dodecane. Unfortunately, GC is not sufficiently soluble in these solvents (see below and Figures S3A-B), even at low concentrations and/or high temperatures, which indicated that this compound forms large aggregates that prevented a proper analysis of the polymerization process. This could be solved, nonetheless, by analyzing good and bad solvent mixtures. Specifically, we performed a set of experiments in which the volume fraction of an alkane (V_a) is increased in mixtures with THF, CHCl_3 or toluene at constant concentration and temperature. Although a similar qualitative outcome is obtained in all of these experiments, no matter the good-bad solvent combination (see Figures S3B-D), the best results were obtained in THF:alkane mixtures.

As V_a is increased, the spectroscopic features that characterize the cyclotetramerization process, as described above in THF and toluene, are first observed. For instance, upon monitoring this process by ^1H NMR at a $3.0 \cdot 10^{-4}$ M concentration (Figure 3a), the residual monomer signals first disappear and the $c\text{GC}_4$ macrocycle is formed quantitatively. When this process was recorded by CD, absorption or emission spectroscopy at similar or lower concentrations (Figures 3b-d; green to purple spectra), we also saw the typical features of $c\text{GC}_4$ formation: a CD signal appears, a red-shifted absorption shoulder, and also a red shift and decrease in emission intensity as the heptane content is increased. Further increasing V_a up to 0.6-0.9 (depending on concentration; see below), produced no spectroscopic change, indicating that the $c\text{GC}_4$ species is quantitatively stabilized in solution.

However, at even higher V_a , a distinct aggregation process is clearly detected (purple to pink spectra). In ^1H NMR, very minor chemical shifts ($\Delta\text{ppm} < 0.05$) are observed and then the $c\text{GC}_4$ proton signals start to broaden and eventually disappear, which is characteristic of the formation of large aggregates. Unfortunately, as shown in Figure 3a, the moment the macrocycles start to aggregate, the proton signal of the peripheral amide also broadens and disappears, which prevented us to monitor intermolecular H-bonding interactions. Turning to optical spectroscopy, an additional absorption red-shift to 425 nm is observed, while emission is further quenched and slightly blue-shifted. However, the most remarkable changes were detected in the CD measurements: at high V_a , the $c\text{GC}_4$ CD features evolve with clear isosbestic points to a new signal exhibiting a Cotton effect at 428 nm, that is positive for *S*-GC and

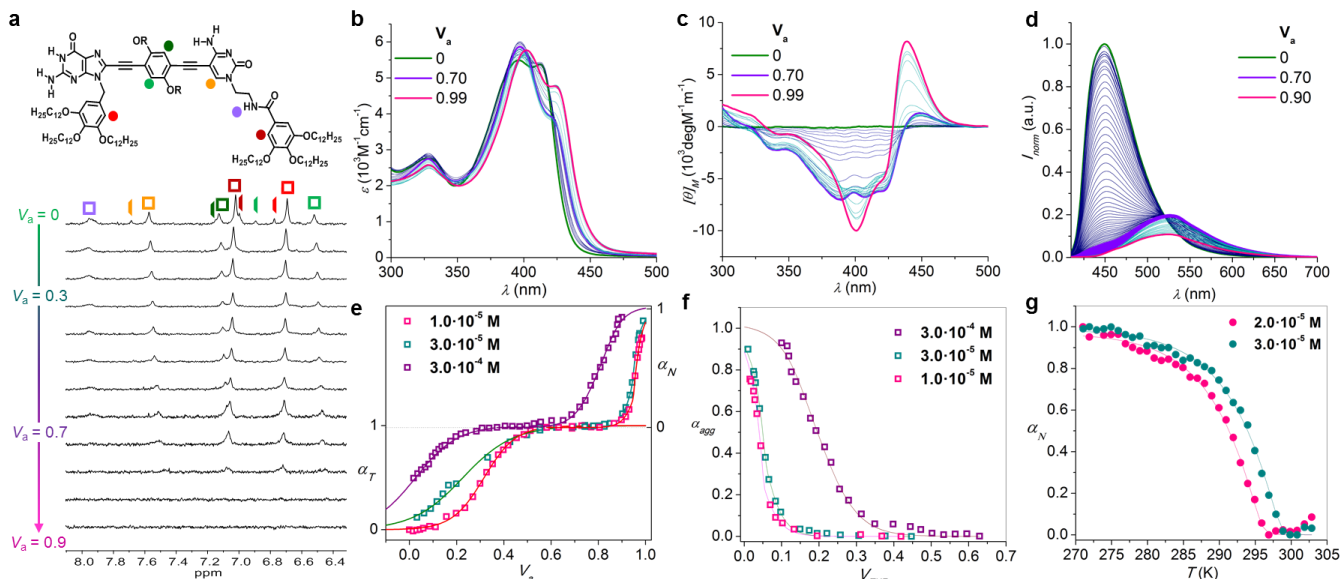


Figure 3. Supramolecular Polymerization. (a-d) Changes observed in the: (a) aromatic region of the ^1H NMR spectra by increasing the volume fraction of cyclohexane- D_{12} (V_a) in mixtures with THF- D_8 ($[\text{GC}] = 3.0 \cdot 10^{-4} \text{ M}$); (b) absorption (c) CD and (d) emission spectra as a function of the volume fraction of heptane (V_a) in mixtures with THF ($[\text{S-GC}] = 3.0 \cdot 10^{-5} \text{ M}$). (e-g) Changes in the S-GC CD signal at 429 nm at several concentrations as a function of (e) volume fraction of heptane (V_a) or (f) volume fraction of THF (V_{THF}) at 298 K or (g) temperature at $V_a = 0.99$ (α_T = fraction of cyclotetramers, α_N = fraction of nanotubes, α_{agg} = fraction of aggregated species).

negative for *R*-GC (Figure S3E). Due to the similarity of these final spectroscopic features at high heptane contents to the ones measured for the initial dispersions in alkanes, this second sharp transition was attributed to a supramolecular polymerization process to yield $(\text{cGC}_4)_n$, which would be driven by π - π stacking interactions between the large π -conjugated surface generated upon cyclization and by H-bonding interactions between the four peripheral amides (see Figure 1c). As a matter of fact, related G-C monomers lacking these amide groups at the C base did not undergo this second self-assembly process, and remained associated as cGC_4 even in pure heptane (see Figure S3F).

Both self-assembly stages, cyclotetramerization and polymerization, are displayed in Figure 3e by monitoring the evolution of the GC CD features as a function of V_a at different concentrations (see also Figure S3G). It is clear that both processes are strongly dependent on the overall concentration. For instance, at $3.0 \cdot 10^{-4} \text{ M}$, we mainly start with a GC- cGC_4 equilibrium that is shifted to the cyclic species up to $V_a = 0.3$, while the polymerization transition is detected above $V_a = 0.65$. At $1.0 \cdot 10^{-5} \text{ M}$, in contrast, we observe the whole two-step self-assembly process: from the monomer in pure THF, to the cGC_4 cycle within the $V_a = 0.5$ - 0.9 plateau, and then to the polymer above $V_a = 0.95$.

Such cGC_4 -(cGC_4) $_n$ transitions as a function of the solvent composition were fitted to an extended nucleation-elongation model developed by de Greef, Meijer and co-workers (Figures 3f and S3G, Tables 1b and S2),⁴¹ which allows the calculation of the Gibbs free energy gain upon monomer addition (ΔG°), the m parameter which characterizes the ability of the good solvent to associate with the

monomer thereby destabilising the supramolecular aggregated species, as well as the equilibrium nucleation (K_n) and elongation (K_e) constants, whose ratio defines the cooperative parameter (σ). A detailed explanation is provided in section S3 of the Supporting Information.

We then turned to temperature-dependent studies in order to obtain complementary thermodynamic parameters for this polymerization process. We fixed solvent composition at $V_a = 0.97$ and analyzed the CD changes along cooling cycles within the 329-268 K range (Figures 3g and S3H). The non-sigmoidal curves obtained at three different concentrations could be fitted again to a cooperative nucleation-elongation model,⁴²⁻⁴⁴ in which the polymerization process can be divided in a nucleation and an elongation phase. The magnitudes T_e (elongation temperature), K_n and K_e (nucleation and elongation constants), σ (cooperativity factor), ΔH_n° and ΔH_e° (nucleation and elongation enthalpies), and ΔS° (polymerization entropy) can be obtained from a non-linear least-square analysis of the experimental melting curves (Tables 1c and S3; see also the Supporting Information, section S3).

The degrees of cooperativity calculated in these experiments are lower than those determined before as a function of solvent composition, but this is not surprising, since each kind of analysis and experimental conditions differ substantially.

Characterization of the Self-assembled Nanotubes.

We then proceeded to characterize the final GC aggregates obtained after the polymerization process, in order to confirm their dimensions and tubular nature. However, solution measurements, like dynamic light scattering (DLS) or

small angle X-ray scattering (SAXS) at high heptane contents faced a challenging scenario, because of the evolution of a third hierarchical assembly level that involves the formation of large bundled agglomerates. In fact, after the polymerization process is complete at high V_a , and in a timescale that depends on concentration (ranging from a few hours to several days), we observed that the solution became turbid and a precipitate appeared. When monitoring this process spectroscopically with time, the shape of the absorption and CD spectra did not change, but a gradual loss in absorption intensity and a baseline rise, attributed to scattering, was noted. Once this final aggregation state is reached, we noted quite marked kinetic effects, and the $(cGC_4)_n$ dispersions are rather inert to disaggregation, so solubilization by heating or dilution required unusually long times.

Despite these experimental difficulties, DLS measurements (Figure S4A) performed at several concentrations and THF:heptane ratios, thus targeting cycle ($V_a = 0.4$) and polymer ($V_a = 0.99$) states, were in agreement with the formation of large anisotropic aggregates at high alkane contents. On the other hand, SAXS experiments, obtained immediately after sample preparation at high V_a , provided an indication of cylindrical organization of large particles. As shown in Figure 4a (black curve) the position of the 1st peak (marked with an arrow) indicates a regular dimension of 3.8 nm, attributed to the distance between bundled cylinder centers, while according to the vague second peak the packing appears hexagonal. However, these SAXS measurements, which required relatively high concentrations, were particularly sensitive to the precipitation process, and the patterns recorded evolved with time (compare black and blue curves in Figure 4a) eventually providing a picture of the smaller particles that remained in solution. In any case, fitting of the data acquired at different time lapses to a cylindrical core-shell model was consistent with a cylinder diameter of 4 ± 1 nm and a core diameter of about 1 nm.

Finally, we analyzed $(S/R-)$ GC samples, drop-casted from diluted solutions with high heptane contents ($V_a > 0.9$), by different microscopy techniques (SEM, AFM and TEM; see Section S4.3). SEM measurements (Figures 4b and S4C) confirmed the formation of networks of large fibrillar aggregates. A closer analysis by TEM (Figures 4c-d) revealed that these aggregates consist of heavily bundled longitudinal objects with a measured diameter of 3.9 ± 0.7 nm, which coincides with the hard aromatic section of the cyclic tetramers (Figure 4e). Organization into aligned nanotube bundles increases as the time in solution before deposition becomes longer (please, compare Figures 4d/S4F and 4c/S4G), and is plausibly driven by van der Waals interactions between interdigitated peripheral chains.

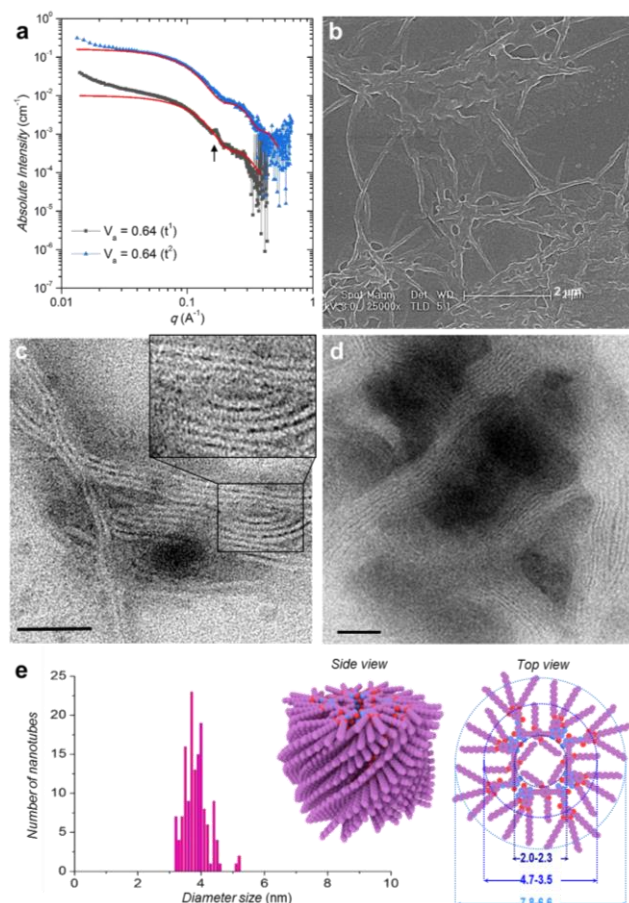


Figure 4. (a) SAXS data and corresponding fits of a 10^{-2} M solution of GC at $V_a = 0.64$ as a function of time ($t^1 \ll t^2$) after sample preparation. (b) SEM (scale bar = 2 μm) and (c,d) TEM (scale bar = 50 nm) images of the assemblies formed by S -GC drop-casted from diluted solutions of high V_a . (e) Nanotube diameter distribution measured by TEM and dimensions calculated from models (see the Supporting Information).

CONCLUSIONS

In short, by means of a novel supramolecular design, which involves H-bonding motifs and cooperative effects of different hierarchy and acting in orthogonal directions, we demonstrated herein that we can guide the assembly of rod-like π -conjugated molecules into precisely defined nanotubular structures through a decoupled two-step process. A cyclotetramerization event, displaying remarkably high chelate cooperativities, takes place first through G:C Watson-Crick pairing. Subsequently, a nucleation-growth polymerization process can be triggered, where the cycle acts as a “supramolecular monomer”. This unprecedented approach may allow access to diverse custom-tailored self-assembled nanotubes by performing small modifications in the monomer structure.

ASSOCIATED CONTENT

Supporting Information. Experimental details, compound synthesis and characterizations, additional spectroscopy and microscopy data and analysis. This material is available free of charge via the Internet at <http://pubs.acs.org>.

AUTHOR INFORMATION

Corresponding Author

*david.gonzalez.rodriguez@uam.es

Notes

The authors declare no competing financial interests.

ACKNOWLEDGMENT

Funding from the European Research Council (ERC-Starting Grant 279548 PROGRAM-NANO) and MINECO (CTQ2014-57729-P and CTQ2017-84727-P) is gratefully acknowledged. V.V.G. is grateful to MINECO for a FPI Grant. I.K.V. would like to acknowledge the Netherlands Organization for Scientific Research (NWO VIDI Grant 723.014.006) for financial support.

REFERENCES

- Hunter, C. A.; Anderson, H. L. What is Cooperativity?. *Angew. Chem. Int. Ed.* **2009**, *48*, 7488-7499.
- Ercolani, G.; Schiaffino, L.; Allosteric, Chelate, and Interanular Cooperativity: A Mise au Point. *Angew. Chem. Int. Ed.* **2011**, *50*, 1762-1768.
- von Krbek, L. K. S.; Schalley, C. A.; Thordarson, P. Assessing Cooperativity in Supramolecular Systems. *Chem. Soc. Rev.* **2017**, *46*, 2622-2637.
- Bharata, T. A. M.; Castillo Menendez, L. R.; Hagen, W. J. H.; Lux, V.; Igonet, S.; Schorb, M.; Schur, F. K. M.; Kräusslich, H. G.; Briggs, J. A. G. Cryo-electron Microscopy of Tubular Arrays of HIV-1 Gag Resolves Structures Essential for Immature Virus Assembly. *Proc. Nat. Acad. Sci.* **2014**, *111*, 8233-8238.
- Dutzler, R. X-ray Structure of a CIC Chloride Channel at 3.0 Å Reveals the Molecular Basis of Anion Selectivity. *Nature* **2002**, *415*, 287-294.
- Komatsu, K.; Qu, X.; Ihara, H.; Fujihara, M.; Azuma, H.; Ikeda, H. Virus Trap in Human Serum Albumin Nanotube. *J. Am. Chem. Soc.* **2011**, *133*, 3246-3248.
- Fyles, T. M. How Do Amphiphiles Form Ion-Conducting Channels in Membranes? Lessons from Linear Oligoesters. *Acc. Chem. Res.* **2013**, *46*, 2847-2855.
- Montenegro, J.; Ghadiri, M. R.; Granja J. R. Ion Channel Models Based on Self-Assembling Cyclic Peptide Nanotubes. *Acc. Chem. Res.* **2013**, *46*, 2955-2965.
- Yuge, S.; Akiyama, M.; Komatsu, T. An Escherichia Coli Trap in Human Serum Albumin Microtubes. *Chem. Commun.* **2014**, *50*, 9640-9643.
- Darnall, S. M.; Li, C.; Dunbar, M.; Alsina, M.; Keten, S.; Helms, B. A.; Xu, T. Organic Nanotube with Subnanometer, pH-Responsive Lumen. *J. Am. Chem. Soc.* **2019**, *141*, 10953-10957.
- Shimizu, L. S.; Salpage, S. R.; Korous, A. A. Functional Materials from Self-Assembled Bis-urea Macrocycles. *Acc. Chem. Res.* **2014**, *47*, 2116-2127.
- Si, W.; Xin, P.; Li, Z.-T.; Hou, J.-L. Tubular Unimolecular Transmembrane Channels: Construction Strategy and Transport Activities. *Acc. Chem. Res.* **2015**, *48*, 1612-1619.
- Shimizu, T.; Masuda, M.; Minamikawa, H. Supramolecular Nanotube Architectures Based on Amphiphilic Molecules. *Chem. Rev.* **2005**, *105*, 1401-1443.
- Hamley, I. W. Peptide Nanotubes. *Angew. Chem. Int. Ed.* **2014**, *53*, 6866-6881.
- Barclay, T. G.; Constantopoulos, K.; Matison, J. Nanotubes Self-Assembled from Amphiphilic Molecules via Helical Intermediates. *Chem. Rev.* **2014**, *114*, 10217-10291.
- Shimizu, T.; Kameta, N.; Ding, W.; Masuda, M. Lipid Nanotubes and Microtubes: Experimental Evidence for Unsymmetrical Monolayer Membrane Formation from Unsymmetrical Bolaamphiphiles. *Langmuir* **2016**, *32*, 12242-12264.
- Shimizu, T. Self-Assembly of Discrete Organic Nanotubes. *Bull. Chem. Soc. Jpn.* **2018**, *91*, 623-668.
- Beingessner, R. L.; Fan, Y.; Fenniri, H. Molecular and Supramolecular Chemistry of Rosette Nanotubes. *RSC Adv.* **2016**, *6*, 75820-75838.
- Mayoral, M. J.; Bilbao, N.; González-Rodríguez, D. Hydrogen-Bonded Macrocyclic Supramolecular Systems in Solution and on Surfaces. *ChemistryOpen* **2016**, *5*, 10-32.
- Adhikari, B.; Lin, X.; Yamauchi, M.; Ouchi, H.; Aratsua, K.; Yagai, S. Hydrogen-bonded Rosettes Comprising π -conjugated Systems as Building Blocks for Functional One-dimensional Assemblies. *Chem. Commun.* **2017**, *53*, 9663-9683.
- Aparicio, F.; Mayoral, M. J.; Montoro-García, C.; González-Rodríguez, D. Guidelines for the assembly of hydrogen-bonded macrocycles. *Chem. Commun.* **2019**, *55*, 7277-7299.
- Davis, J. T. G-quartets 40 Years Later: from 5'-GMP to Molecular Biology and Supramolecular Chemistry. *Angew. Chem. Int. Ed.* **2004**, *43*, 668-698.
- Dash, J.; Saha, P. Functional architectures derived from guanine quartets. *Org. Biomol. Chem.* **2016**, *14*, 2157-2163.
- Yagai, S.; Goto, Y.; Lin, X.; Karatsu, T.; Kitamura, A.; Kuzuhara, D.; Yamada, H.; Kikkawa, Y.; Saeki, A.; Seki, S. Self-Organization of Hydrogen-Bonding Naphthalene Chromophores into J-type Nanorings and H-type Nanorods: Impact of Regioisomerism. *Angew. Chem. Int. Ed.* **2012**, *51*, 6643-6647.
- Adhikari, B.; Yamada, Y.; Yamauchi, M.; Wakita, K.; Lin, X.; Aratsu, K.; Ohba, T.; Karatsu, T.; Hollamby, M.; Shimizu, N.; Takagi, H.; Haruki, R.; Adachi, S.; Yagai, S. Light-induced Unfolding and Refolding of Supramolecular Polymer Nanofibers. *Nat. Commun.* **2017**, *8*, 15254.
- Jonkheijm, P.; Miura, A.; Zdanowska, M.; Hoebe, F. J. M.; Jonkheim, P.; De Feyter, S.; Schenning, A. P. H. J.; De Schryver, F. C.; Meijer, E. W. π -Conjugated Oligo-(p-phenylenevinylene) Rosettes and Their Tubular Self-Assembly. *Angew. Chem. Int. Ed.* **2004**, *43*, 74-78.
- Yagai, S.; Usui, M.; Seki, T.; Murayama, H.; Kikkawa, Y.; Uemura, S.; Karatsu, T.; Kitamura, A.; Asano, A.; Seki, S. Supramolecularly Engineered Perylene Bisimide Assemblies Exhibiting Thermal Transition from Columnar to Multilamellar Structures. *J. Am. Chem. Soc.* **2012**, *134*, 7983-7994.
- Cafferty, B. J.; Gállego, I.; Chen, M. C.; Farley, K. I.; Eritja, R.; Hud, N. V. Efficient Self-Assembly in Water of Long Non-covalent Polymers by Nucleobase Analogues. *J. Am. Chem. Soc.* **2013**, *135*, 2447-2450.
- Mascal, M. C.; Farmer, S. C.; Arnall-Culliford, J. R. Synthesis of the G-C DNA Base Hybrid with a Functional Tail. *J. Org. Chem.* **2006**, *71*, 8146-8150.
- Johnson, R. S.; Yamazaki, T.; Kovalenko, A.; Fenniri, H. Molecular Basis for Water-Promoted Supramolecular Chirality Inversion in Helical Rosette Nanotubes. *J. Am. Chem. Soc.* **2007**, *129*, 5735-5743.
- Bilbao, N.; Destoop, I.; De Feyter, S.; González-Rodríguez, D. Two-Dimensional Nanoporous Networks Formed by Liquid-to-Solid Transfer of Hydrogen-Bonded Macrocycles Built from DNA Bases. *Angew. Chem. Int. Ed.* **2016**, *55*, 659-663.
- Montoro-García, C.; Camacho-García, J.; López-Pérez, A. M.; Bilbao, N.; Romero-Pérez, S.; Mayoral, M. J.; González-Rodríguez, D. High-fidelity Noncovalent Synthesis of Hydrogen-bonded Macrocyclic Assemblies. *Angew. Chem. Int. Ed.* **2015**, *54*, 6780-6784.
- Romero-Pérez, S.; Camacho-García, J.; Montoro-García, C.; López-Pérez, A. M.; Sanz, A.; Mayoral, M. J.; González-

- Rodríguez, D. G-Arylated Hydrogen-Bonded Cyclic Tetramer Assemblies with Remarkable Thermodynamic and Kinetic Stability. *Org. Lett.* **2015**, *17*, 2664–2667.
- (34) Montoro-García, C.; Camacho-García, J.; López-Pérez, A. M.; Mayoral, M. J.; Bilbao, N.; González-Rodríguez, D. Role of the Symmetry of Multipoint Hydrogen Bonding on Chelate Cooperativity in Supramolecular Macrocyclization Processes. *Angew. Chem. Int. Ed.* **2016**, *55*, 223–227.
- (35) Montoro-García, C.; Mayoral, M. J.; Chamorro, R.; González-Rodríguez, D. How Large Can We Build a Cyclic Assembly? Impact of Ring Size on Chelate Cooperativity in Noncovalent Macrocyclizations. *Angew. Chem. Int. Ed.* **2017**, *56*, 15649–15653.
- (36) Chamorro, R.; de Juan-Fernández, L.; Nieto-Ortega, B.; Mayoral, M. J.; Casado, S.; Ruiz-González, L.; Pérez, E. M.; González-Rodríguez, D. Reversible Dispersion and Release of Carbon Nanotubes *via* Cooperative Clamping Interactions with Hydrogen-bonded Nanorings. *Chem. Sci.* **2018**, *9*, 4176–4184.
- (37) Montoro-García, C.; Bilbao, N.; Tsagri, I. M.; Zaccaria, F.; Mayoral, M. J.; Guerra, C. F.; González-Rodríguez, D. Impact of Conformational Effects on the Ring–Chain Equilibrium of Hydrogen-Bonded Dinucleosides. *Chem. Eur. J.* **2018**, *24*, 11983–11991.
- (38) Mayoral, M. J.; Serrano-Molina, D.; Camacho-García, J.; Magdalena-Estirado, E.; Blanco-Lomas, M.; Fadaei, E.; González-Rodríguez, D. Understanding Complex Supramolecular Landscapes: Non-covalent Macrocyclization Equilibria Examined by Fluorescence Resonance Energy Transfer. *Chem. Sci.* **2018**, *9*, 7809–7821.
- (39) Camacho-García, J.; Montoro-García, C.; López-Pérez, A. M.; Bilbao, N.; Romero-Pérez, S.; González-Rodríguez, D. Synthesis and Complementary Self-association of Novel Lipophilic π -conjugated Nucleoside Oligomers. *Org. Biomol. Chem.* **2015**, *13*, 4506–4513.
- (40) Mayoral, M. J.; Camacho-García, J.; Magdalena-Estirado, E.; Blanco-Lomas, M.; Fadaei, E.; Montoro-García, C.; Serrano-Molina, D.; González-Rodríguez, D. Dye-conjugated Complementary Lipophilic Nucleosides as Useful Probes to Study Association Processes by Fluorescence Resonance Energy Transfer. *Org. Biomol. Chem.* **2017**, *15*, 7558–7565.
- (41) Korevaar, P. A.; Schaefer, C.; de Greef, T. F. A.; Meijer, E. W. Controlling Chemical Self-Assembly by Solvent-Dependent Dynamics. *J. Am. Chem. Soc.* **2012**, *134*, 13482–13491.
- (42) Maarkvort, A. J.; Ten Eikelder, H. M. M.; Hilbers, P. J. J.; De Greef, T. F. A.; Meijer, E. W. Theoretical models of nonlinear effects in two-component cooperative supramolecular copolymerizations. *Nat. Commun.* **2011**, *2*, 509.
- (43) Ten Eikelder, H. M. M.; Markwoort, A. J.; De Greef, T. F. A.; Hilbers, P. A. J. An equilibrium model for chiral amplification in supramolecular polymers. *J. Phys. Chem. B* **2012**, *116*, 5291–5301.
- (44) Rest, C.; Kandaneli, R.; Fernández, G. Strategies to create hierarchical self-assembled structures via cooperative non-covalent interactions. *Chem. Soc. Rev.* **2015**, *44*, 2543–2572.

